Molecular beam photoelectron spectroscopy and femtosecond intramolecular dynamics of H_2O^+ and D_2O^+

J. E. Reutt, L. S. Wang, Y. T. Lee, and D. A. Shirley
Materials and Molecular Research Division, Lawrence Berkeley Laboratory and Department of Chemistry, University of California, Berkeley, California 94720

(Received 11 April 1986; accepted 9 September 1986)

The 584 Å photoelectron spectra of supersonic molecular beams of H_2O and D_2O have been obtained with improved resolution. The spectroscopic constants of the $\tilde{X}\,^2B_1$ and $\tilde{A}\,^2A_1$ state ions, including ω_1^0, x_{11}^0, ω_2^0, x_{22}^0, and x_{12}^0, are reported. For the first two electronic states of the ion, precise line splittings were evaluated with a least squares fitting procedure, employing sums of empirical instrument response functions and a linear background. A simulation of the vibrational manifolds of the $\tilde{B}\,^2B_2$ state ions with combination progressions in the symmetry-allowed modes ν_1 and ν_2 failed to reproduce the diffuse photoelectron bands observed for both H_2O and D_2O. Autocorrelation functions were calculated from the photoelectron bands of all three electronic states. The $\tilde{B}\,^2B_2$ state correlation functions exhibit ultrafast decay, occurring on a 10^{-14} s time scale. The ν_2 motion appears to define the decay in the correlation function. This behavior supports a previously proposed $\tilde{B}\,^2B_2$–$\tilde{A}\,^2A_1$ curve-crossing model for the nonradiative relaxation of the $\tilde{B}\,^2B_2$ state ions.

I. INTRODUCTION

The importance of the H_2O molecule in atmospheric and interstellar chemistry has prompted a series of studies of the spectroscopy, photodissociation, photoionization, and fragmentation behavior of both the neutral and ionic species. The H_2O molecule and its isotopic variants have several attributes which render them particularly interesting for study by photoelectron spectroscopy. The equilibrium geometry of the first three electronic states of H_2O^+ are vastly different. The ionic ground $\tilde{X}\,^2B_1$ state possesses an equilibrium geometry close to that of the neutral ground state, with an H–O–H bond angle (θ_{HOH}) of 110.46° and an O–H bond length (R_{OH}) of 0.9988 Å.[1] The first electronically excited $\tilde{A}\,^2A_1$ ionic state has been determined to be near linear, with bond length $R_{OH} = 0.98(1)$ Å.[2–4] The second electronically excited ionic state, labeled $\tilde{B}\,^2B_2$, possesses the same C_{2v} symmetry as the ground ionic state, but theoretical calculations indicate a much contracted equilibrium bond angle, $\theta_{HOH} = 54.98°$, and an expanded bond length, $R_{OH} = 1.140$ Å.[5]

The wide variation between the equilibrium geometries of the $\tilde{A}\,^2A_1$ and $\tilde{B}\,^2B_2$ state ions and the neutral $\tilde{X}\,^2A_1$ state molecule leads to extensive vibrational progressions in the photoelectron bands. Direct photoionization thus provides a method for preparing "superexcited" species of H_2O^+. The $\tilde{A}\,^2A_1$ and $\tilde{B}\,^2B_2$ state ions contain 1.21 and 4.56 eV of internal electronic energy, respectively, and the Franck–Condon envelope includes states with up to ~3 eV of internal vibrational energy. These superexcited species are then subject to relaxation processes. In cases where the decay occurs on a time scale of 2×10^{-13} s or faster, the photoelectron bands will, in principle, manifest spectral broadening indicative of the intramolecular dynamics of these superexcited states. By applying an autocorrelation function formalism to the interpretation of such photoelectron bands, one can infer the intramolecular dynamics of the ions occurring on a 0–200 fs time scale.

The photoionization of water and the behavior of the molecular ion in its various electronic states has a history of experimental and theoretical treatment. The complete 584 Å (21.2175 eV) photoelectron spectrum at a resolution of over 20 meV FWHM was first reported by Brundle and Turner.[6] Subsequent higher resolution studies, also on room temperature samples, have been published by Dixon, Duxbury, Rabalais, and Asbrink[7] as well as by Karlsson, Mattsson, Jadray, Albridge, Pinchas, Bergmark, and Siegbahn.[8] Because the first photoelectron band, which corresponds to the $\tilde{X}\,^2B_1$ electronic state, is formed by the removal of an electron of nonbonding oxygen $2p_\pi$ character, a contracted vibrational manifold consisting of combinations of the ν_1 (symmetric stretch) and ν_2 (symmetric bend) modes is observed. Individual vibrational levels display unresolved rotational structure, resulting in broad and asymmetric peak shapes. The second photoelectron band, corresponding to the $\tilde{A}\,^2A_1$ electronic state, exhibits an extended ν_2 progression, which is perturbed by strong vibronic coupling (Renner–Teller effect) to the $\tilde{X}\,^2B_1$ state. The photoelectron ejected from the $3a_1$ orbital is emitted from a nominally oxygen $2p$ orbital directed along the C_{2v} molecular axis. This orbital, however, is actually "*sp*" hybridized, so that the oxygen nucleus does not lie in a nodal plane, unlike the $1b_1$ and $1b_2$ orbitals. Consequently, the $3a_1$ orbital alone among the outer valence molecular orbitals would tend to make H_2O nonlinear through bonding. The third photoelectron band, corresponding to the $\tilde{B}\,^2B_2$ state, has a very irregular and complex band profile. Loss of an electron from the $1b_2$ orbital, which contains the oxygen nucleus in its nodal plane, permits the hydrogens to move together to exploit stronger bonding through the $3a_1$ orbital. An angular contraction for the $\tilde{B}\,^2B_2$ state results and the principal features in the band have been assigned to combination anharmonic progressions in the symmetry-allowed modes ν_1 and ν_2, together with unresolved rotational structure.

Photoionization mass spectrometry studies of H_2O over the 600–1000 Å region revealed that the threshold for frag-

 0021-9606/86/246928-12$02.10

mentation to form OH^+ (18.11 eV), H^+ (18.72 eV), and O^+ (18.65 eV) all occur above the adiabatic ionization potential for the $\tilde{B}\,^2B_2$ state.[9] The $\tilde{A}\,^2A_1 \rightarrow \tilde{X}\,^2B_1$ emission spectrum has been detected[1] and the absolute lifetimes of these $\tilde{A}\,^2A_1$ levels have been reported at $10.5(1.0)\times10^{-6}$ s for H_2O^+ and approximately 12% longer for D_2O^+.[10,11] No fluorescence has been reported from the $\tilde{B}\,^2B_2$ state of either ion.

The nonradiative decay of $\tilde{B}\,^2B_2$ state H_2O^+ has been the subject of several theoretical investigations. Fiquet-Fayard and Guyon originally interpreted the production of fragment ions from the $\tilde{B}\,^2B_2$ state as indications of predissociation via spin-orbit coupling to the repulsive $^4A_2$, $^4A''$ state (OH^+ formation) and via spin-orbit and Coriolis coupling to the repulsive $^2A''$ state (H^+ formation).[12] In a more detailed study Lorquet and Lorquet calculated the dissociation probabilities and lifetime of the $\tilde{B}\,^2B_2$ state.[13] They ascribed the complex photoelectron band to a strong vibrational interaction among quasidegenerate transitions and attributed the broad spectral features to a vibrational scrambling that precedes predissociation. They concluded that the predissociation occurred on a 10^{-10}–10^{-13} s time scale, which is too slow to broaden the spectra significantly. A subsequent photoelectron–photoion coincidence study by Eland, however, measured the experimental relative abundances of D_2O^+, OD^+, and D^+ arising from the $\tilde{B}\,^2B_2$ state of D_2O^+ at 584 Å.[13] The D^+ ions were more abundant than predicted by the model of Lorquet and Lorquet. Internal conversion from the $\tilde{B}\,^2B_2$ state to the $\tilde{X}\,^2B_1$ or $\tilde{A}\,^2A_1$ states by vibronic coupling and subsequent fragmentation was proposed to explain the discrepancy in D^+ abundance.

A number of potential energy surface calculations have appeared to the low-lying electronic states of H_2O^+.[3–5,15–17] Balint-Kurti and Yardley first demonstrated the presence of a conical intersection between the $\tilde{A}\,^2A_1$ and $\tilde{B}\,^2B_2$ states with valence–bond calculations. A large scale *ab initio* configuration-interaction potential energy surface study by Jackels, employing double-zeta quality basis sets augmented with polarization functions, examined the detailed effects of the $\tilde{A}\,^2A_1$–$\tilde{B}\,^2B_2$ intersection on the potential energy surfaces. The energy minimum of the curve crossing on the $\tilde{B}\,^2B_2$ surface occurs just 0.0099 hartrees (0.27 eV) above the $\tilde{B}\,^2B_2$ surface minimum. This corresponds to the geometry with a $\theta_{HOH} = 74.4°$ and $R_{OH} = 1.084$ Å. This crossing was predicted to perturb the lower-lying levels of the $\tilde{B}\,^2B_2$ state. A recent dynamical study of the nonadiabatic coupling between the surfaces has been reported by Dehareng, Chapuisat, Lorquet, Galloy, and Raseev.[18] Classical trajectory calculations on the upper adiabatic potential energy surface and nonadiabatic transition probabilities were used to evaluate the rate constant(s) for the $\tilde{B}\,^2B_2 \rightarrow \tilde{A}\,^2A_1$ transitions. At short times two distinct processes were characterized by rate constants on the order of 10^{-14} s. Trajectories through the seam of intersection were most efficient in enabling surface transitions, and a dependence on internal energies was calculated for the transition rates. The $\tilde{B}\,^2B_2 \rightarrow \tilde{A}\,^2A_1$ curve-crossing mechanism was predicted to be at least competitive with the previously proposed vibrational scrambling/electronic predissociation mechanism.

In order to identify experimentally the femtosecond intramolecular dynamics of the low-lying electronic states of H_2O^+ and D_2O^+, we have reexamined the 584 Å photoelectron spectra. Using a supersonic molecular beam source to rotationally cool the molecules, we have obtained higher resolution spectra than previously available, and applied an autocorrelation function formalism to interpret the results dynamically. The vibrational structure in all three photoelectron bands is revealed in greater detail and spectroscopic constants of improved accuracy are reported. Autocorrelation functions for the $\tilde{X}\,^2B_1$, $\tilde{A}\,^2A_1$, and $\tilde{B}\,^2B_2$ state ions describe the motion of the initially prepared wave packets on the upper potential energy surfaces. The $\tilde{X}\,^2B_1$ state correlation function exhibits a stable oscillatory pattern. The Renner–Teller perturbation of the $\tilde{A}\,^2A_1$ state, on the other hand, promotes a rapid phase randomization of the vibrational components of the initially coherent wave packet, resulting in a damped correlation function. The $\tilde{B}\,^2B_2$ state correlation function exhibits an ultrafast decay, which is attributed to nonradiative relaxation and is compared with the theoretical models for the decay of the $\tilde{B}\,^2B_2$ state.

The details of the experiment are described in Sec. II of this paper. A description and the method for calculating the autocorrelation functions follows in Sec. III. Spectroscopic results and the dynamical interpretation are discussed for each electronic state of H_2O^+ and D_2O^+ in Sec. IV. The principal conclusions are then summarized in Sec. V.

II. EXPERIMENTAL

The complete photoelectron spectra of H_2O and D_2O were obtained with a resolution of 11 meV FWHM, as measured for Ar $^2P_{3/2}$. The molecular beam photoelectron spectrometer consists of a 90° spherical sector prefilter, a 180° hemispherical analyzer, associated electron optics, and multichannel detection. It has been described in detail.[19] The electrons are collected at a 90° angle with respect to the incident photon beam and the supersonic molecular beam and the intensity is uncorrected for angular distribution effects. (This has no bearing on our interpretation.) The H_2O β values for $h\nu = 584$ Å have been reported for the $\tilde{X}$, $\tilde{A}$, and $\tilde{B}$ states as 0.99(8), 0.68(5), and $-0.11(3)$, respectively.[20] This yields a relative preference ratio for the collection of $\tilde{X}$:$\tilde{A}$:$\tilde{B}$ electrons of roughly 1.0:0.9:0.8 for the unpolarized radiation employed for this experiment.

High purity water was prepared by passing deionized water through a Barnstead Hose–Nipple cartridge filter to remove trace oxygen, organic, and ionic impurities. The filtrate was then distilled and placed in a reservoir, which was cooled to 0 °C. High purity (>99.999%) helium was passed through the reservoir, producing a gaseous mixture of 1.2% H_2O seeded in helium. This mixture was expanded at a stagnation pressure of 400 Torr through a 0.2 mm diam nozzle, which was at room temperature. These conditions were found to optimize rotational cooling, while restricting the formation of cluster species $[(H_2O)_x]$. The molecular beam was characterized with 584 Å photoionization and a quadrupole mass filter (Extranuclear Laboratories). Under these conditions the presence of <1% clusters was verified by

monitoring the mass ratios of the H_2O^+ and H_3O^+ signals in the mass spectrum.

D_2O (99.8% purity Aldrich) was used without further purification. High purity helium was passed through a room temperature reservoir of D_2O. A mixture of 3.7% D_2O seeded in helium was expanded at a stagnation pressure of 400 Torr through a 0.2 mm diam nozzle, which was held at a temperature of 45 °C. Under these conditions efficient rotational cooling and the presence of $<1\%$ clustered species were observed.

In order to improve the statistics for these dilute conditions and maintain a resolution of 11 meV FWHM, the photoelectron bands were obtained separately. Each photoelectron band was multiply recorded as two sequential scans of the electron kinetic energy. The reported H_2O photoelectron bands each represent the summation of 11 scans. Individual scans were obtained over a time period of less than 1.5 h and each scan was immediately preceded and followed by rare-gas calibration scans. The reported D_2O photoelectron bands represent the summation of eight such spectra. Restricting the length of individual scans limits the total drift in the electron kinetic energy scale to <2 meV.

Scan widths were determined by measuring the voltage of the power supply controlling the kinetic energy with a computer-interfaced precision digital voltmeter (Dana 5900) at four points during the scan. The linearity of the kinetic energy scale was determined by obtaining the N_2 photoelectron spectrum and comparing the N_2^+ $\tilde{X}\,^2\Sigma_g^+$, $v=0$ and $\tilde{B}\,^2\Sigma_u^+$, $v=0$ splitting with the accurate value of 3.169 81 eV obtained from the N_2^+ optical emission spectrum.[21] At higher kinetic energies the linearity of the energy scale was determined from photoelectron spectra of xenon and krypton. A comparison of the ionization potentials of these rare gases and the accurate literature values, Ar $^2P_{3/2}$ I.P. = 15.759 75 eV and Xe $^2P_{3/2}$ I.P. = 12.130 00 eV,[22] indicates an energy scale linear to ± 1 meV over the entire energy range of this experiment. The combined systematic error of the drift and linearity of the energy scale limits the accuracy at which the absolute ionization potentials may be reported to ± 4 meV. Other spectroscopic constants are obtained as line splittings, however, and may be reported to much higher accuracy.

III. THE CORRELATION FUNCTION

Through the time-energy uncertainty principle and under the Born–Oppenheimer approximation, the time evolution of an initially formed vibrational wave packet may be described by an autocorrelation function. This autocorrelation function can be derived from an absorption spectrum with appropriate Fourier transform techniques.[23] Several recent papers have applied the autocorrelation function formalism to the complex polyatomic photoelectron spectra of HCN,[24] C_2H_4,[25] C_2H_2, and C_2D_2.[26] In cases where an ultrafast decay occurs from the initially prepared state the autocorrelation function exhibits an exponential decay. The time scale for this decay can be related to the vibrational motion and, supported with theoretical calculations of the potential energy surface, provides a description of the femtosecond intramolecular dynamics of the excited-state ion.

The time scale for which the autocorrelation function is reliable is determined by the instrumental resolution (presently 11 meV FWHM), the ability to deconvolute the instrument response function, and the signal/noise ratio. In this experiment, an effective resolution, after correcting for these effects, of 3 meV leads to a time window of greater than 200 fs for each electronic state. In the case of the $\tilde{B}\,^2B_2$ spectra, however, the signal/noise ratio reduces this window to 80 fs. Since time and energy are conjugate variables, the extensive photoelectron bands reported for all three electronic states of H_2O^+ and D_2O^+ correspond to an equivalent time resolution of a fraction of a femtosecond.

The autocorrelation function may be expressed as

$$C(t) = |\langle \phi(0) | \phi(t) \rangle|. \tag{1}$$

Here $C(t)$ represents the probability amplitude at time t that the system remains in the initially prepared system and ϕ is the nuclear wave function of the wave packet produced on the upper potential energy surface. A derivation of the autocorrelation function $C(t)$ from the experimentally accessible cross section $\sigma(E)$ has been reported,[24] and only the principal points will be outlined here. The form for the photoelectron cross section may be expressed under a strict Franck–Condon approximation as

$$\sigma(E) \propto |M_{ei}(R,E)|^2 |\langle \psi'' | \psi' \rangle|^2, \tag{2}$$

where $M_{ei}(R,E)$ is the electronic transition moment, a function of the nuclear coordinates R and electron kinetic energy E, and ψ'' and ψ' are the initial- and final-state vibrational wave functions, respectively. The electronic transition moment $M_{ei}(R,E)$ does not vary appreciably over a photoelectron band, and is generally treated as a constant, averaged over the nuclear coordinates and the electron kinetic energy. By applying the completeness relation to the set of eigenstates ψ'' of a molecular Hamiltonian and invoking the analytical expression for the Dirac δ function it has been shown[24] that the cross section becomes

$$\sigma(E) \propto \frac{1}{2\pi} \int_{-\infty}^{+\infty} e^{iEt/\hbar} \langle \psi'' | e^{-iEt/\hbar} | \psi'' \rangle dt. \tag{3}$$

In this expression ψ'' is identified as the initial nuclear wave function $\phi(0)$, and $e^{-iEt/\hbar}|\psi''\rangle$ as $\phi(t)$. Making these substitutions yields

$$\sigma(E) \propto \frac{1}{2\pi} \int_{-\infty}^{+\infty} e^{iEt/\hbar} \langle \phi(0) | \phi(t) \rangle dt. \tag{4}$$

The correlation function may then be obtained by a Fourier transform of the cross section

$$C(t) = |\langle \phi(0) | \phi(t) \rangle| \propto \frac{1}{2\pi} \int_{-\infty}^{+\infty} e^{-iEt/\hbar} \sigma(E) dE. \tag{5}$$

Prior to an evaluation of the correlation function, it is necessary to calculate $\sigma(E)$ from the quantity $I(E)$, intensity vs energy, which we measure. This is accomplished by deconvoluting the instrument response function, which we determine from the photoelectron spectrum of a rare gas at a kinetic energy comparable to the band of interest. In the present case the Kr $^2P_{3/2}$ line was selected for the $\tilde{X}\,^2B_1$ state, while the Ar $^2P_{3/2}$ line was appropriate for the $\tilde{A}\,^2A_1$ and $\tilde{B}\,^2B_2$ states.

In order to obtain a pure vibrational correlation function, it is necessary to account for a residual rotational temperature present in the sample following the supersonic expansion. This is achieved by convoluting the rare-gas instrumental response function with a narrow Gaussian, since the cold rotational temperature produces symmetric line shapes, but the rotational selection rules and finite rotational constants effect some broadening. (For all three low-lying electronic states of H_2O^+ and D_2O^+, $\Delta N = \pm 1$, and ΔK_a and ΔK_c for the $\tilde{X}$, $\tilde{A}$, and $\tilde{B}$ states are ± 1 and 0; ± 1 and ± 1; and 0 and ± 1, respectively.[27]) The rotationally broadened instrument function for each ionic species was first determined for the ground ionic state, since the rotational constants, selection rules, and long time stability of this molecular ionic state are well known. For the $\tilde{X}\,^2B_1$ state of H_2O^+, a Kr $^2P_{3/2}$ empirical instrument function was convoluted with a 15 meV Gaussian. The ground state of D_2O^+ required a convolution of Kr $^2P_{3/2}$ and an 11 meV Gaussian to obtain the rotationally broadened instrument function. The monotonic long-time behavior of the autocorrelation functions calculated for the state of each ion supported this choice of instrument function. For the $\tilde{B}\,^2B_2$ state, the Ar $^2P_{3/2}$ empirical instrument function was convoluted with a 15 and 11 meV Gaussian, respectively, to produce the rotationally corrected instrument function for H_2O^+ and D_2O^+. Since the $\tilde{A}\,^2A_1$ state has near-$D_{\infty h}$ symmetry, and possesses considerably smaller rotational constants than the two C_{2v} states, the Ar $^2P_{3/2}$ line was convoluted with narrower 8 and 6.5 meV Gaussians to obtain the rotationally corrected instrument functions for H_2O^+ and D_2O^+, respectively.

The procedure for calculating correlation functions for the three low-lying ionic states of each isotopic species is now summarized. Each photoelectron band was isolated and the empirically determined background, plus any constant background, were removed. Each resulting band was normalized, designated $I(E)$ below, and Fourier transformed with a discrete fast Fourier transform algorithm.[28] The effect of the instrument response function and residual rotational temperature was then removed for each band. This was achieved by dividing the product of separate fast Fourier transforms of the instrument response function, designated $I_{RG}(E)$, and a narrow Gaussian, designated $g(E)$, into the Fourier-transformed photoelectron band. The autocorrelation function is then obtained from the modulus of the quotient. The complete procedure, as applied to the photoelectron band of each accessible electronic state, is represented below:

$$C^{\text{vib}}(t) = \left| \int_{-\infty}^{+\infty} I(E) e^{-iEt/\hbar}\, dE \Big/ \left\{ \int_{-\infty}^{+\infty} I_{RG}(E) e^{-iEt/\hbar}\, dE \times \int_{-\infty}^{+\infty} g(E) e^{-iEt/\hbar}\, dE \right\} \right|. \tag{6}$$

The shape of $C(t)$ is determined by the magnitude of self-overlap of the initially prepared coherent ensemble of vibrational levels comprising the wave packet. The harmonic motion of the vibrational wave packet is revealed by the oscillatory form of the correlation function. It provides a "clock" for the intramolecular dynamics under investigation. Since photoionization is intrinsically a nonresonant process, the wave packet formed is not composed of a single eigenstate of the molecular Hamiltonian, but an ensemble of eigenstates. In the case of a triatomic molecule, therefore, the population of both symmetry-allowed modes ν_1 and ν_2 introduces the complication of a beat pattern in the correlation function. The phase relationship and relative populations of the two vibrational modes determines the form of the beat pattern. Fortunately, for the triatomic H_2O^+ and D_2O^+ systems the vibrational beat pattern is relatively simple. This enables a clear distinction between effects which can be ascribed to stable anharmonic motion within a bound potential, and effects which represent an ultrafast ($\approx 10^{-14}$ s) decay of the initially prepared wave packet. The shape of $C(t)$ is thus a measure of the femtosecond intramolecular dynamics of these electronic states.

IV. RESULTS AND DISCUSSION

Results of the three low-lying electronic states of H_2O^+ and D_2O^+ are discussed separately below. Table I presents a summary of our measured spectroscopic constants, together with optically determined values previously reported in the literature.

A. $\tilde{X}\,^2B_1$ state

The isolated photoelectron bands of the $\tilde{X}\,^2B_1$ state of each ion are displayed in Fig. 1. The C_{2v} geometry of this state has been accurately determined by emission spectroscopy[1] and the more intense vibrational features have been reported and assigned by the earliler photoemission studies. In the present work, rotational cooling enables all of the observed vibrational levels to be determined with improved accuracy and the mean energies of these transitions were determined by the following least squares fitting procedure. The adiabatic transitions were first determined by fitting these features to Gaussians. The adiabatic peaks were then isolated and used as empirical functions to fit the successive vibrational levels. The procedure allows the values of peak splitting to be determined to an accuracy of $\leqslant 0.0003$ eV. The mean transitions located through this fitting procedure are listed in Table II. The levels were then fitted to the standard expression[29]

$$G_0(v_1,v_2,v_3) = \sum_i^3 \omega_i^0 v_i + \sum_i^3 \sum_{k>i}^3 x_{ik}^0 v_i v_k, \tag{7}$$

where

$$\omega_i^0 = \omega_i + x_{ii}^0 + \frac{1}{2} \sum_{k \neq i} x_{ik}^0, \tag{8}$$

and ω_i and x_{ik}^0 are zero point vibrational frequencies and quadratic anharmonicity constants, respectively.

Absolute adiabatic ionization potentials for the $\tilde{X}\,^2B_1$ state of H_2O^+ and D_2O^+ are 12.6224(4) and 12.6395(4) eV, respectively. The H_2O^+ $\tilde{X}\,^2B_1$ surface along the bending and the symmetric stretching coordinates is described by $\omega_2^0 = 1433.7(4.0)\ \text{cm}^{-1}$ and $x_{22}^0 = -24.0(2.0)\ \text{cm}^{-1}$, and $\omega_1^0 = 3270.6(4.0)\ \text{cm}^{-1}$ and $x_{11}^0 = -65.0(2.0)\ \text{cm}^{-1}$. The

TABLE I. Spectroscopic constants determined for the first three electronic states of H_2O^+ and D_2O^+ from high resolution molecular beam photoelectron spectroscopy. All units in cm^{-1} unless noted.

	H_2O^+	D_2O^+
$\tilde{X}\,^2B_1$		
A.I.P.[a] (eV)	12.6223(3)	12.6395(3)
ω_1^0, x_{11}^0	3270.6(4.0), − 65.3(2.0)	2373.9(4.0), − 30.0(2.0)
ω_2^0, x_{22}^0	1433.7(4.0), − 24.0(2.0)	1078.(4.0), − 25.4(2.0)
	1431.173, − 22.768[1]	
x_{12}^0	− 22(5)	− 23(5)
$\tilde{A}\,^2A_1$		
ν_1	3547(16)	2531(8)
ω_2^0, x_{22}^0	868(8), 5.6(5)	643(4), 2.8(5)
	870.9, 5.93[1]	
x_{12}^0	− 33(8)	− 15(4)
$\tilde{B}\,^2B_2$		
A.I.P.[a] (eV)	17.178(1)	17.411(1)
ω_1^0, x_{11}^0	3024, − 56	2282, 0
ω_2^0, x_{22}^0	1637, − 41	117, − 18

[a] Errors of the absolute adiabatic ionization potentials (A.I.P.) are ± 0.004 eV. The smaller errors referring to the relative positions of the transitions and peak splittings are noted parenthetically.

H_2O^+ ω_2 values determined from the $v_2 = 0$–2 range by Lew[1] as $\omega_2^0 = 1431.173\ cm^{-1}$ and $x_{22}^0 = -22.768\ cm^{-1}$ are in good agreement. The D_2O^+ $\tilde{X}\,^2B_1$ surface is characterized by $\omega_2^0 = 1078.8(4.0)\ cm^{-1}$ and $x_{22}^0 = -25.4(2.0)\ cm^{-1}$ and $\omega_1^0 = 2373.9(4.0)\ cm^{-1}$ and $x_{11}^0 = -30.0(2.0)\ cm^{-1}$. The anharmonic coupling of the ν_1 and ν_2 modes is identified by $x_{12}^0 = -22(5)\ cm^{-1}$ for H_2O^+ and $x_{12}^0 = -23(5)\ cm^{-1}$ for D_2O^+.

The correlation functions calculated from the $\tilde{X}\,^2B_1$ state of each ion are shown in Fig. 2. Similar oscillatory patterns are observed for each isotopic species. This type of pattern results from the phase relationship of a stable two mode anharmonic oscillator system, in which $\nu_1 \geqslant 2\nu_2$. At shorter times a dephasing of the wave packet dominates the correlation function. After 10.4 fs for H_2O^+ (14.0 fs for D_2O^+) the fastest components of the wave packet return to the origin and a reduced maximum of 0.79 (0.70 for D_2O^+) is achieved. This corresponds closely to one period of ν_1 motion. The slower components of the wave packet, which must also travel along the ν_2 coordinate, are expected to return to the origin after approximately one period of ν_2 motion. The observed maxima in correlation of 0.90 at 21.2 fs and 0.88 at 29.0 fs for H_2O^+ and D_2O^+, respectively, are largely attributed to this return. The small shifts in the times of the observed peaks in the correlation function arise from a spreading of the wave packet in the anharmonic potential and the relative phase relationship between the ν_1 and ν_2 oscillation.

High correlation is retained at longer times (> 0.7 at 150 fs), which is indicative of the stability of the wave pack-

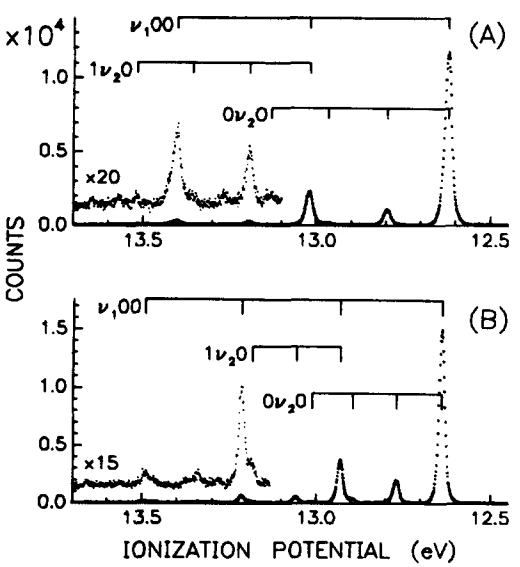

FIG. 1. The rotationally cold He I (584 Å) $\tilde{X}\,^2B_1$ photoelectron bands of H_2O (A) and D_2O (B). The observed ionic vibrational progressions are indicated in the figure.

TABLE II. Ionization potentials (eV), relative intensities, and assignment of the vibrational transitions of the $\tilde{X}\,^2B_1$ photoelectron bands of H_2O and D_2O.

	H_2O		D_2O	
Assignment	I.P.[a]	Intensity	I.P.[a]	Intensity
0 0 0	12.6223(3)	1.000	12.6395(3)	1.000
0 1 0	12.7967(3)	0.089	12.7691(4)	0.135
0 2 0	12.9663(5)	0.010	12.8953(5)	0.002
1 0 0	13.0197(3)	0.193	12.9299(4)	0.253
0 3 0	13.1288(4)	0.003	13.0123(5)	0.006
1 1 0	13.1918(3)	0.016	13.0577(4)	0.037
1 2 0	13.3583(5)	0.003	13.1846(5)	0.009
2 0 0	13.4009(4)	0.023	13.2145(4)	0.042
1 3 0	13.5192(5)	0.002		
2 1 0	13.5694(5)	0.003	13.3400(4)	0.004
2 2 0			13.4695(5)	0.002
3 0 0			13.4900(4)	0.005

[a] Errors of absolute ionization potentials (I.P.'s) are ± 0.004 eV. The smaller errors referring to the relative positions of the transitions are noted parenthetically.

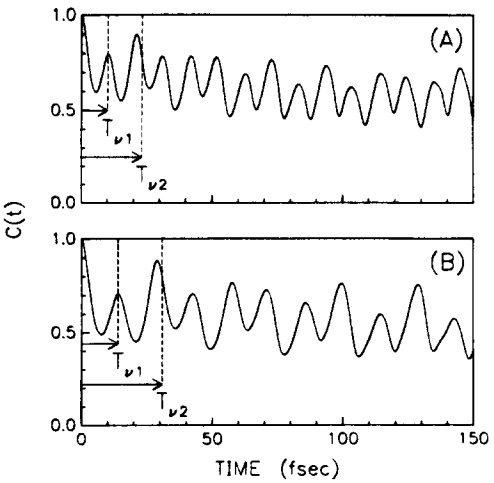

FIG. 2. The correlation functions calculated for the ground $\tilde{X}\,^2B_1$ state of H_2O^+ (A) and D_2O^+ (B). The periods of ν_1 and ν_2 harmonic motion, designated T_{ν_1} and T_{ν_2}, respectively, describe the oscillatory form of the stable wave packet.

et. Relatively shallow minima are observed in the correlation function, which is a characteristic of a wave packet prepared through a predominantly adiabatic transition. In such cases the initially prepared wave packet is localized about the minimum of the upper potential energy surface and weakly oscillates about this region, retaining substantial correlation at all times.

B. $\tilde{A}\,^2A_1$ state

The vibronic structure of the $\tilde{A}\,^2A_1$ state photoelectron band has been interpreted as arising from a Renner–Teller effect.[1,6–8] Both the $\tilde{A}\,^2A_1$ and $\tilde{X}\,^2B_1$ states correlate with the orbitally degenerate $^2\Pi_u$ state of the linear geometry with ± 1 values for Λ, the projection of the electronic orbital angular momentum on the internuclear axis. The ν_2 and K dependence of the vibrational coupling of the two states is manifested as a splitting of the vibronic sublevels of the $\tilde{A}\,^2A_1$ state. The vibronic sublevels observed for each quantum of ν_2 correspond to the possible values of K, the resultant of the electronic angular momentum Λ, and the vibrational angular momentum l. The even quanta of ν_2 correspond to the vibronic sublevels $K = 1,3,5,\ldots,l-1$ (labeled $\Pi,\Phi,G,\ldots$) and the odd quanta to the sublevels $K = 0,2,4,\ldots,l-1$ (labeled $\Sigma,\Delta,\Gamma,\ldots$). The $\tilde{A}\,^2A_1 \rightarrow \tilde{X}\,^2B_1$ emission spectrum[1] has provided a detailed characterization of many of the rovibronic transitions over the $\nu_2 = 5$–15 range for the $\tilde{A}$ state. In room temperature photoelectron spectra, it was possible to discern alternating linewidths in the ν_2 progression. The broad peaks were attributed to Π sequences and the sharper features to Σ sequences. This pattern was explained by the overlapping rotational contours of the vibronic subcomponents.

The isolated photoelectron bands of the rotationally cold species are presented in Figs. 3 and 4. A significant modification of the $\tilde{A}\,^2A_1$ state photoelectron band profile is obtained through rotationally cooling the sample, and two distinct progressions become apparent for each isotopic species. The Σ sequences become the broadest features, forming a distinct progression, and the sharper Π sequences com-

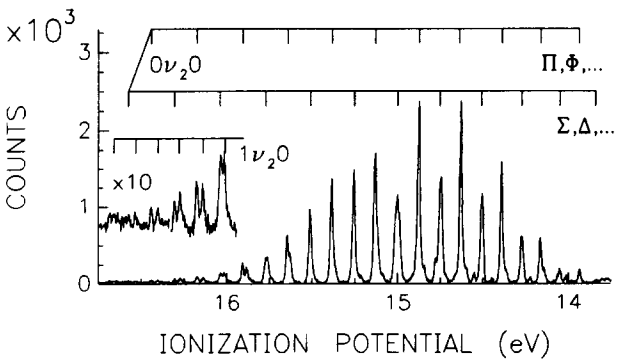

FIG. 3. The rotationally cold He I (584 Å) $\tilde{A}\,^2A_1$ state photoelectron band of H_2O. The dominant ν_2 progression may be separated into two progressions of even ($\Sigma,\Delta,\ldots$) and odd ($\Pi,\Phi,\ldots$) vibronic sublevels. At higher ionization potentials the combination progression $[1,\upsilon_2,0]$ becomes apparent.

prise a second progression. This is consistent with a Σ–Δ splitting of $\sim 120\,\mathrm{cm}^{-1}$ (14.8 meV) and a larger, resolvable Π–Φ splitting of $\sim 220\,\mathrm{cm}^{-1}$ (28 meV), which was reported by Lew for the limited $\upsilon_2 = 5$–15 range. A second vibrational progression is evident at higher ionization potentials and is assigned to the combination progression $[1,\upsilon_2,0]$.

The fitting procedure described below was used to locate the mean peak energies of the principal vibronic sublevels and obtain refined spectroscopic constants, subcomponent splittings, and subcomponent relative intensities over the extended $\upsilon_2 = 1$–24 ($\upsilon_2 = 3$–26 for D_2O^+) range of the photoelectron bands. A rotationally broadened instrument function was first generated for each isotopic species by fitting an isolated vibronic sublevel [$\upsilon_2 = 1$, $K = 1(\Pi)$ for H_2O^+ and $\upsilon_2 = 3$, $K = 1(\Pi)$ for D_2O^+] to Ar $^2P_{3/2}$ peak convoluted with a Gaussian. The resulting functions, Ar $^2P_{2/3}$ convoluted with an 8.0 meV FWHM Gaussian for H_2O^+ and Ar $^2P_{3/2}$ convoluted with a 6.5 meV FWHM Gaussian for D_2O^+, and a linear background were then used to fit the photoelectron bands. The number of parameters included in the fit was restricted by including three or fewer vibronic sublevels for each $[0,\upsilon_2,0]$ level. The empirical form given by Dressler,[31] $\nu_0^K = \nu_0 - GK^2$, where G is an empirical constant, was used to locate higher K sublevels. These transitions were only weakly observed, permitting this truncation of fitting parameters. The procedure was further simplified by fitting each $[1,\upsilon_2,0]$ feature to a single peak. These transi-

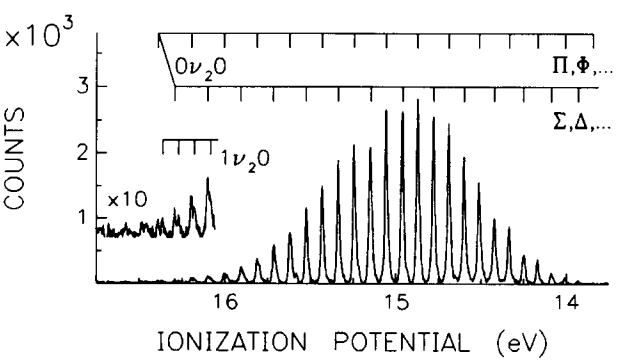

FIG. 4. The rotationally cold He I (584 Å) $\tilde{A}\,^2A_1$ state photoelectron band of D_2O. The vibronic sublevels are noted in the figure.

tions are also subject to a Renner–Teller splitting, but they are too weak to permit the evaluation of more than the multiplet centroid from the present experiment. The results of this fitting procedure are summarized in Table III. The quality of the fit is demonstrated for several vibrational levels in Fig. 5.

Only the Σ sublevels are not vibronically coupled to the $\tilde{X}\,^2B_1$ state,[29] and these transitions were used to evaluate the ν_2 spectroscopic constants. We determine $\omega_2^0 = 868(8)$ cm^{-1} and $x_{22}^0 = 5.6(5)$ cm^{-1} for H_2O^+ and $\omega_2^0 = 643(4)$ cm^{-1} and $x_{22}^0 = 2.8(5)$ cm^{-1} for D_2O^+. These values are consistent with the H_2O^+ constants of $\omega_2^0 = 870.9$ cm^{-1} and $x_{22}^0 = 5.93$ cm^{-1} determined over the restricted $v_2 = 5$–15 range by Lew. Our H_2O^+ Σ–Δ splitting over the $v_2 = 5$–15 range is 102(20) cm^{-1} and the Π–Φ splitting is evaluated as 195(50) cm^{-1}. The observed splittings of the vibronic subcomponents, however, as well as the relative intensity ratios of the vibronic subcomponents, i.e., Σ/Δ and Π/Φ, are quite erratic. These effects can be explained by a strong Fermi interaction between the $[1,v_2-3,0]$ and $[0,v_2,0]$ vibrational levels. Extrapolating the $[1,v_2,0]$ progression, which is distinguished at higher vibrational levels, down to lower levels in the potential indicates that this $[1,v_2,0]$ progression will be appropriately positioned to perturb strongly the more intense $[0,v_2,0]$ progression.

The frequency of ν_1 may also be determined from combination differences between the $[1,v_2,0]$ and $[0,v_2,0]$ transitions. The $[1,v_2,0]$ progression weakly shadows the principal ν_2 progression for lower $[0,v_2,0]$ levels and is of

TABLE III. Ionization potentials (eV), relative intensities, and assignment of the principal vibrational transitions observed in the $\tilde{A}\,^2A_1$ photoelectron bands of H_2O and D_2O.

Assignment		H_2O I.P.[a]	H_2O Intensity	D_2O I.P.[a]	D_2O Intensity
0 1 0		13.8417	0.011		
0 2 0	Π	13.9388	0.069	13.8452	0.004
0 3 0	Δ	14.0455	0.025		
0 3 0	Σ	14.0507	0.051	13.9309	0.019
1 0 0		14.0633	0.025		
0 4 0	Φ	14.1410	0.071	13.9949	0.008
0 4 0	Π	14.1637	0.244	14.0091	0.034
1 1 0		14.1731	0.020		
0 5 0	Γ	14.2239	0.031		
0 5 0	Δ	14.2643	0.113	14.0755	0.025
0 5 0	Σ	14.2744	0.222	14.0889	0.055
1 2 0		14.2856	0.022		
0 6 0	Φ	14.3652	0.068	14.1472	0.017
0 6 0	Π	14.3908	0.671	14.1688	0.134
1 3 0		14.4032	0.033		
0 7 0	Γ	14.4475	0.025	14.2163	0.005
0 7 0	Δ	14.5025	0.406	14.2430	0.085
0 7 0	Σ	14.5114	0.216	14.2532	0.129
1 4 0		14.5217	0.042		
0 8 0	G	14.5530	0.056		
0 8 0	Φ	14.6022	0.078	14.3140	0.027
0 8 0	Π	14.6398	1.000	14.3350	0.260
1 5 0		14.6519	0.036	14.3441	0.094
0 9 0	Γ			14.3708	0.010
0 9 0	Δ	14.7420	0.474	14.4081	0.093
0 9 0	Σ	14.7540	0.387	14.4231	0.350
1 6 0		14.7771	0.121	14.4360	0.055
0 10 0	Φ	14.8470	0.077	14.5011	0.118
0 10 0	Π	14.8749	0.986	14.5129	0.519
1 7 0		14.8905	0.134	14.5235	0.062
0 11 0	Δ	14.9862	0.286	14.5817	0.089
0 11 0	Σ	15.0010	0.4257	14.6000	0.708
1 8 0		15.0154	0.271	14.6152	0.052
0 12 0	G	15.0872	0.041		
0 12 0	Φ	15.1130	0.198	14.6782	0.179
0 12 0	Π	15.1303	0.693	14.6906	0.864
1 9 0		15.1400	0.132	14.7053	0.065
0 13 0	Γ	15.2160	0.029		
0 13 0	Δ	15.2380	0.031	14.7607	0.083
0 13 0	Σ	15.2544	0.613	14.7785	0.966
1 10 0		15.2679	0.085	14.7935	0.129
0 14 0	Φ	15.3643	0.079	14.8591	0.299
0 14 0	Π	15.3840	0.554	14.8727	1.000
1 11 0		15.3942	0.085		
0 15 0	Δ	15.4980	0.076	14.9357	0.064
0 15 0	Σ	15.5101	0.371	14.9591	0.797
1 12 0		15.5214	0.055	14.9677	0.360
0 16 0	Φ	15.6256	0.136	15.0408	0.177
0 16 0	Π	15.6437	0.243	15.0567	0.996
1 13 0		15.6522	0.036		
0 17 0	Γ	15.7356	0.025	15.0721	0.052
0 17 0	Δ	15.7575	0.121	15.1294	0.074
0 17 0	Σ	15.7720	0.119	15.1444	0.552
0 14 0		15.7838	0.020		
0 18 0	G	15.8595	0.015	15.2172	0.065
0 18 0	Φ	15.8818	0.080	15.2336	0.192
0 18 0	Π	15.9064	0.106	15.2449	0.734
0 19 0	Γ	15.9875	0.009		
1 16 0		16.0113	0.047		
0 19 0	Δ	16.0286	0.035	15.3217	0.078
0 19 0	Σ	16.0402	0.033	15.3367	0.684
1 17 0		16.1384	0.025	15.4011	0.022
0 20 0	Φ			15.4205	0.134
0 20 0	Π	16.1738	0.032	15.4316	0.530
0 21 0	Γ	16.2688	0.013	15.5102	0.084
1 18 0		16.2797	0.010		
0 21 0	Σ	16.3054	0.013	15.5247	0.425
1 19 0		16.4010	0.015		
0 22 0	Φ			15.6092	0.145
0 22 0	Π	16.4400	0.011	15.6215	0.268
0 23 0	Δ			15.6953	0.058
1 20 0		16.5320	0.007	15.7095	0.120
0 23 0	Σ	16.5750	0.005	15.7170	0.129
1 21 0		16.659	0.004	15.7979	0.082
0 24 0	Π			15.8123	0.127
1 22 0				15.8927	0.043
0 25 0	Σ			15.9067	0.084
1 23 0				15.9896	0.026
0 26 0	Π			16.0050	0.050
1 24 0				16.0828	0.025
0 27 0	Σ			16.0998	0.052
1 25 0				16.1760	0.019
0 28 0	Π			16.1953	0.030
1 26 0				16.2696	0.014
0 29 0	Σ			16.2921	0.017
1 27 0				16.3627	0.012
0 30 0	Π			16.3899	0.009

[a] Errors of absolute ionization potentials (I.P.'s) are $\pm$ 0.004 eV. The relative transition energies, however, may be evaluated with a much higher accuracy ($\pm$ 0.0005 eV).

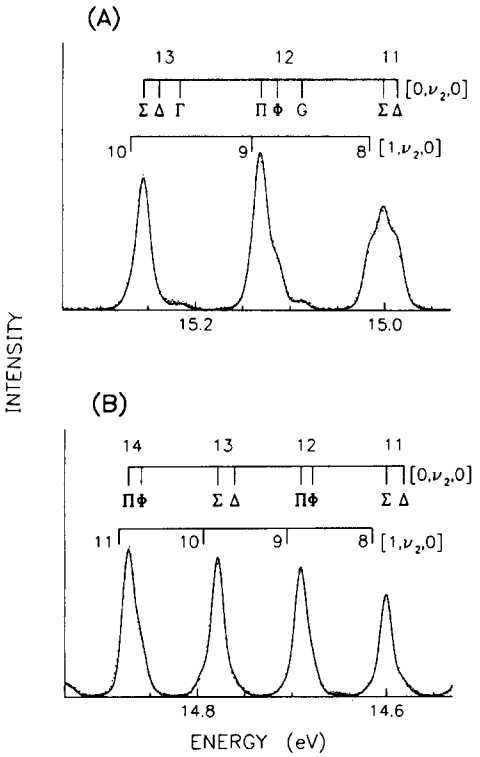

FIG. 5. A portion of the $\tilde{A}\,^2A_1$ state photoelectron bands of H_2O (A) and D_2O (B) are shown together with the results of a least squares fit to a sum of empirically determined instrument response functions and a linear background. The assigned vibronic sublevels are designated in the figure.

comparable intensity only for higher levels. Combination differences between $[1,v_2,0]$ and $[0,v_2,0]$ for $v_2 = 16$–20 yields $\nu_1 = 3547(16)$ cm^{-1} for H_2O^+. The D_2O^+ $\nu_1 = 2531(12)$ cm^{-1} frequency is obtained from combination differences over the $v_2 = 23$–26 range.

The calculated correlation functions for the $\tilde{A}\,^2A_1$ state are presented in Fig. 6. The wave packet formed by photoionization is strongly displaced from the $\tilde{A}\,^2A_1$ state potential minimum. Accordingly, the wave packet quickly moves from the initially occupied region of phase space and the correlation function drops to zero. After 16.5 fs, or roughly one half-period of ν_2 bending motion, a correlation of 0.11 is achieved for H_2O^+. The peaks at half-integral periods of ν_2 are attributed to a phase change initiated by the Renner–Teller coupling of the $K > 0$ sublevels of the $\tilde{A}\,^2A_1$ state to the $\tilde{X}\,^2B_1$ state. A sharply peaked correlation of 0.78 at 33.2 fs represents a completed ν_2 period. As the wave packet continues to evolve, the peaks in the correlation function become distorted and lose intensity. This loss of correlation reflects the phase randomization induced by the varied Renner–Teller coupling of the vibronic subcomponents. As time evolves further, the deep minima in the correlation function become filled in by the quickly spreading wave packet.

The D_2O^+ correlation function exhibits very similar behavior. A sharp maximum of 0.76 at 44.8 fs closely corresponds to one period of ν_2 motion within this potential of positive anharmonicity. The subsequent decay in correlation and concurrent increase in peak width for the correlation function occur more slowly than for H_2O^+, however. This represents a weaker Renner–Teller coupling of the $\tilde{A}\,^2A_1$ state to the $\tilde{X}\,^2B_1$ state for D_2O^+ and, consequently, a slower phase randomization.

C. $\tilde{B}\,^2B_2$ state

The photoelectron bands corresponding to the removal of a $1b_2$ electron are shown in Fig. 7. The O–H bonding and H–H antibonding character of this orbital leads to an equilibrium structure with a contracted bond angle and increased bond length. The resulting photoion should exhibit strongly excited ν_1 and ν_2 modes on the basis of Franck–Condon considerations. These progressions have been used to assign the dominant features in the room temperature photoelectron bands.[6,8] Despite the rotational cooling and

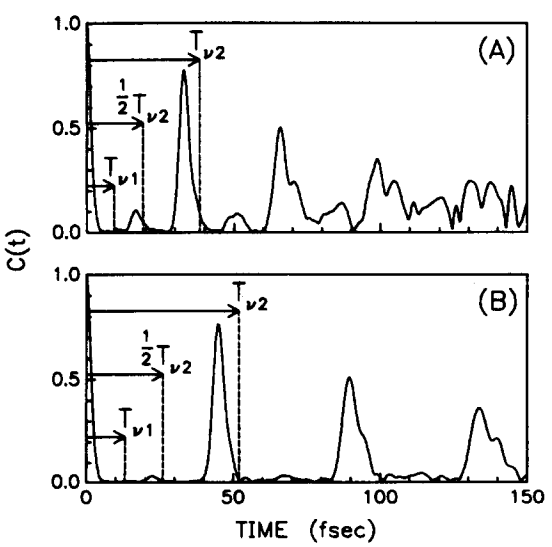

FIG. 6. The correlation functions calculated for the first excited $\tilde{A}\,^2A_1$ states of H_2O^+ (A) and D_2O^+ (B). At shorter times the correlation function is sharply peaked, in relationship to the periods of ν_2 motion, T_{ν_2}. A phase randomization at longer times, induced by the $\tilde{A}\,^2A_1$–$\tilde{X}\,^2B_1$ Renner–Teller coupling, causes a spreading and splitting of the wave packet.

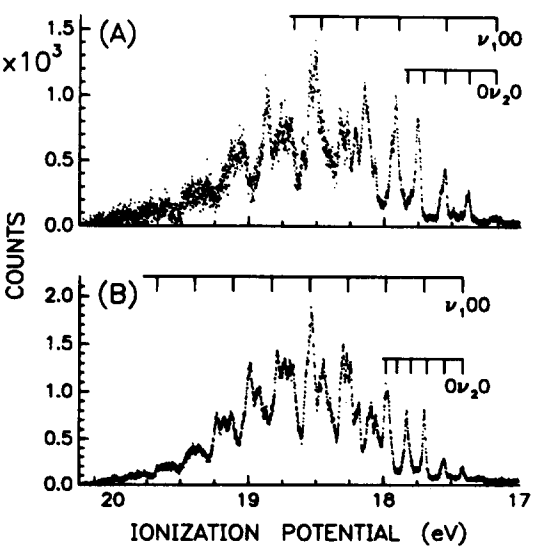

FIG. 7. The rotationally cold He I (584 Å) $\tilde{B}\,^2B_2$ state photoelectron bands of H_2O (A) and D_2O (B). The principal ν_1 and ν_2 progressions, indentified through a simulation of the vibrational manifolds, are designated in the figure.

improved resolution of the present spectra, diffuse bands and erratic intensity patterns continue to be observed.

The extent to which these cold bands deviate from a two-mode anharmonic oscillator system has been evaluated by simulating the measured bands with a vibrational manifold consisting of combinations of ν_1 and ν_2. The asymmetric stretching mode ν_3 is omitted from the simulation on the basis of Franck–Condon arguments and photoionization selection rules, which permit ν_3 to be weakly populated in integrals of two quanta only. Within the adiabatic approximation, this asymmetric mode is estimated to contribute $<2\%$ of the intensity in the observed spectrum *by direct photoionization*. For each isotopic species, the simulation is done by fitting the peaks near the potential minimum (I.P.'s <18.5 eV) to their respective rotationally broadened instrument functions. This identifies the adiabatic ionization potentials, ν_1 and ν_2 frequencies uncorrected for anharmonicities, and the relative intensity patterns of the two progressions near the potential minimum. The full bands were then generated by extending the range of the vibrational progressions, including anharmonicity, and optimizing the intensities and spectroscopic constants to produce line spectra. The relative intensities of the pure ν_1 and ν_2 progressions were entered as distinct parameters, but the combination band intensities, i.e., $I[n,m,0]$, where n = the number of quanta in ν_1 and m = the number of quanta in ν_2, were taken as products of the intensities entered for the nth level of mode ν_1 and the mth level of mode ν_2. Finally, the resulting line spectra were convoluted with the rotationally broadened instrument functions. The simulated photoelectron bands are plotted together with the experimental bands in Fig. 8. The parameters used in these simulations are tabulated in Table IV. The H_2O^+ $\tilde{B}\,^2B_1$ state is best described by $\omega_1^0 = 3024\ \text{cm}^{-1}$ and $x_{11}^0 = -56\ \text{cm}^{-1}$ and $\omega_2^0 = 1637\ \text{cm}^{-1}$ and $x_{22}^0 = -41\ \text{cm}^{-1}$. The D_2O^+ $\tilde{B}\,^2B_1$ state exhibits less anharmonicity, with $\nu_1 = 2282\ \text{cm}^{-1}$, $\omega_2^0 = 1117\ \text{cm}^{-1}$, and $x_{22}^0 = -18\ \text{cm}^{-1}$.

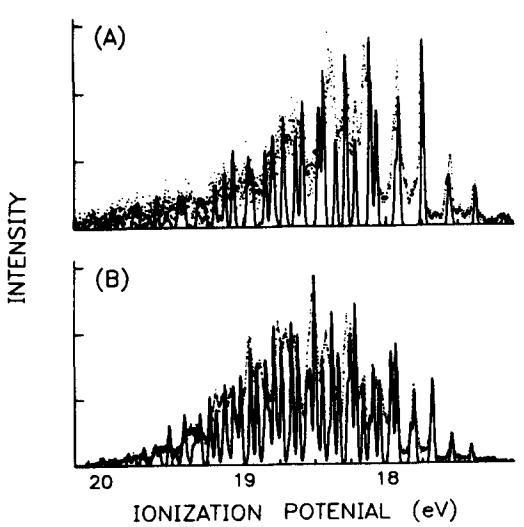

FIG. 8. Simulations of the vibrational manifolds of the $\tilde{B}\,^2B_2$ state photoelectron bands (line) are compared to the recorded photoelectron bands (dot) for H_2O (A) and D_2O (B). The anharmonic normal mode description fails to reproduce the observed spectral density.

TABLE IV. Parameters used to simulate the $\tilde{B}\,^2B_2$ photoelectron spectra of H_2O and D_2O.

	H_2O		D_2O	
A.I.P. (eV)	17.178		17.411	
ω_1^0, x_{11}^0 (cm^{-1})	3024, −56		2282,0	
ω_2^0, x_{22}^0 (cm^{-1})	1637, −41		1117, −18	
	Relative intensities			
	H_2O^+		D_2O^+	
Vibrational level	ν_1	ν_2	ν_1	ν_2
0	0.68		0.26	
1	0.76	0.26	0.32	0.24
2	0.39	0.35	0.37	0.68
3	0.15	1.000	0.27	0.73
4	0.10	0.87	0.10	1.00
5	0.09	0.83	0.04	0.70
6	0.04	0.61	0.02	0.65
7	0.02	0.56	0.01	0.51
8	0.01	0.43		0.30
9		0.26		0.16
10		0.11		0.11
11		0.06		0.08
12		0.03		0.08
13		0.02		0.05
14		0.01		0.03

The general band shapes are reproduced by this two anharmonic mode simulation. The erratic intensity patterns appear, moreover, to originate from the combination vibrational structure. Yet, both experimental spectra are considerably more diffuse than their simulated counterparts. At ionization potentials $\geqslant 17.8$ eV, it appears that dynamical models must be invoked to interpret the density of observed transitions. If an intramolecular energy transfer process occurs on an ultrafast time scale, the emitted photoelectron will be sensitive to the changing potential. The discrete vibrational levels prepared at time $t = 0$ become obscured by the relaxation process, and information concerning the decay is contained in the photoelectron bands. The energy spectra indicate which levels are involved in the relaxation, and the autocorrelation functions indicate the time scales for the relaxation.

A comparison of the recorded and simulated spectra suggests that the $\tilde{B}\,^2B_2$ state ions of both isotopic species with ionization potentials $\geqslant 17.8$ eV are involved in the ultrafast intramolecular dynamics. The spectral diffusiveness appears to "turn on" for ions with internal energies $\geqslant 0.6$ eV, and extends throughout the entire Franck–Condon region representative of higher internal energies.

The autocorrelation functions calculated for the $\tilde{B}\,^2B_2$ state of H_2O^+ and D_2O^+, respectively, appear in Figs. 9 and 10. A sharp initial decline in the correlation function from time $t = 0$ for H_2O^+ is followed by weak maxima of 0.09 and 0.13 at times of 9.7 and 20.2 fs, respectively, corresponding to periodic motion along the ν_1 and ν_2 coordinates. This loss of correlation is significantly greater than expected solely from a dephasing of the wave packet, and indicates that intramolecular energy transfer has occurred in less than one

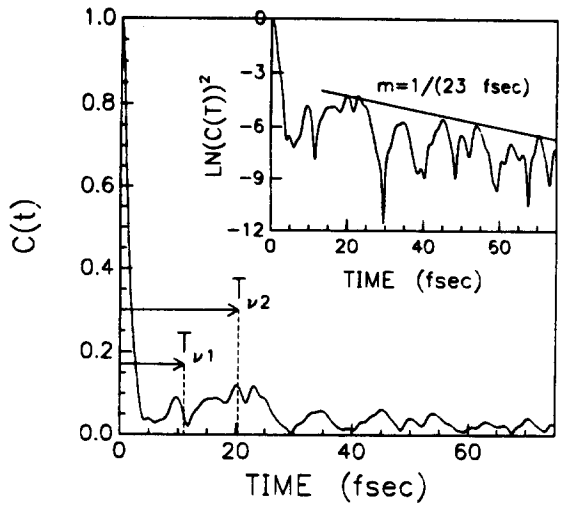

FIG. 9. The correlation function calculated for the $\tilde{B}\,^2B_2$ state of H_2O^+. A sharp drop in correlation is observed from time $t = 0$, representing the combined effects of wave packet dephasing and ultrafast decay. The subsequent decay is monitored from the slope of $\ln[C(t)^2]$ (see inset), which closely matches a single period of ν_2 motion.

period of vibrational motion. Following this initial wave packet dephasing and commensurate decay, the subsequent decay of the wave packet may be evaluated qualitatively from the slope of $\ln[C(t)^2]$. A decay time of 23 fs, or approximately one period of ν_2 motion, is observed. The D_2O^+ correlation function mirrors this behavior on the slightly longer time scale of its vibrational periods. After the initial decay in correlation, a maximum of only 0.13 is reached at 17.8 fs. The subsequent decay evaluated from $\ln[C(t)^2]$ occurs in 32 fs, again close to one period of D_2O^+ ν_2 motion. The rate of decay of the $\tilde{B}\,^2B_2$ state ions, therefore, appears to correspond to the bending motion for each isotopic species.

The theoretical models which have been proposed to explain the $\tilde{B}\,^2B_2$ state relaxation behavior are now considered. The first model employs ultrafast vibronic coupling and Fermi resonances among quasidegenerate levels of the

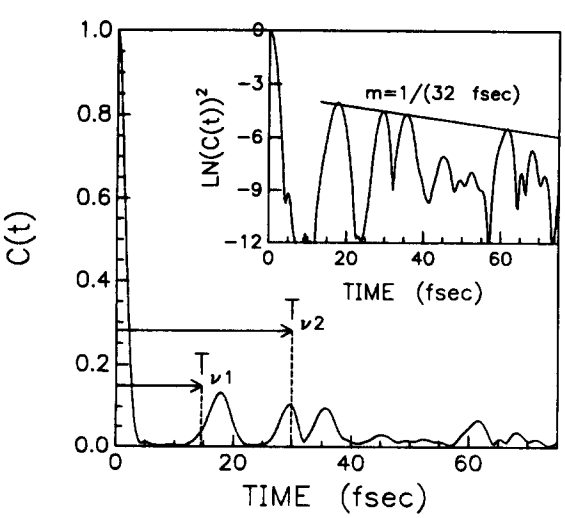

FIG. 10. The correlation function calculated for the $\tilde{B}\,^2B_2$ state of D_2O^+. As for H_2O^+, a sharp drop in correlation is observed from time $t = 0$. The subsequent decay evaluated from the slope of $\ln[C(t)^2]$ (see inset) closely corresponds to a single period of ν_2 motion.

$\tilde{B}\,^2B_2$ state to populate ν_1 levels.[13] These ν_1 levels can subsequently predissociate on an $\approx 10^{-10}$ s time scale by repulsive $^4A''$ and $^2A''$ states. This model explains the diffuse photoelectron band structure above ≈ 18.0 eV, the asymptotic dissociation limit for the $^4A''$ state, but the assumption of complete redistribution among quasidegenerate vibrational levels is very drastic. This redistribution model is statistical and should retain 30%–40% of the wave packet in its initially prepared distribution. The autocorrelation functions indicate that substantially less of the initially prepared distribution is actually thus retained. Furthermore, as noted in the Introduction, this model cannot reproduce the observed D^+ fragmentation (and presumably H^+) pattern identified in the photoelectron–photoion coincidence studies.[14]

The second model considers the $\tilde{B}\,^2B_2$ and $\tilde{A}\,^2A_1$ state curve crossing. A schematic representation of the diabatic $\tilde{A}\,^2A_1$ and $\tilde{B}\,^2B_2$ potential energy surfaces is given in Fig. 11. The energy minimum of the surface crossing has been evaluated as lying at 0.27 eV above the minimum of the $\tilde{B}\,^2B_2$ potential energy surface. This corresponds to a bond angle of $\theta = 74.4°$ and a bond length of $R_{OH} = 1.106$ Å.[16] The wave packet is conceived on the $\tilde{B}\,^2B_2$ surface and initially propagates along this surface. Trajectories which pass near the seam of intersection of the two surfaces can efficiently hop over to the $\tilde{A}\,^2A_1$ surface. The ν_2 mode thus facilitates the curve crossing, while the ν_1 mode restricts the curve crossing by pushing the wave packet trajectories further from the seam of intersection. Dehareng *et al.* identify two curve-

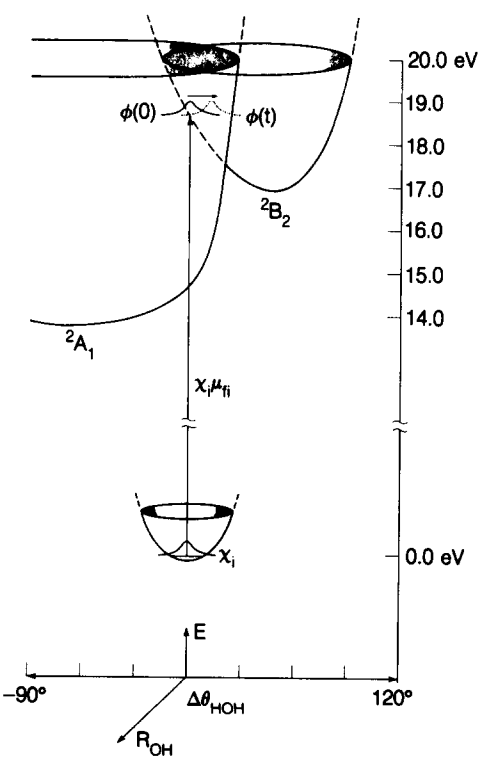

FIG. 11. The $\tilde{B}\,^2B_2$–$\tilde{A}\,^2A_1$ curve-crossing model for the nonradiative decay of the $\tilde{B}\,^2B_2$ state is depicted schematically. The diabatic $\tilde{B}\,^2B_2$ and $\tilde{A}\,^2A_1$ surfaces cross near the $\tilde{B}\,^2B_2$ minimum. The wave packet $\phi(0)$ is prepared on the $\tilde{B}\,^2B_2$ surface by photoionization. As the wave packet travels along the Δ_{HOH} (or ν_2) coordinate it passes through the seam of intersection and can hop over to the $\tilde{A}\,^2A_1$ surface.

crossing processes, both of which occur on time scales on the order of 10^{-14} s.[18] The first process includes states which undergo an efficient curve crossing in less than one period of ν_2 motion. The second process includes those states with some ν_1 excitation. The latter states approach the intersecting seam later, do not pass directly through the seam, and undergo a branching in the vicinity of the curve crossing. As time evolves further, depopulation of the $\tilde{B}\,^2B_2$ state becomes slower, for the wave packet becomes depleted of components with higher transition probabilities for crossing over to the $\tilde{A}\,^2A_1$ surface.

The calculated correlation functions are consistent with the curve-crossing model for $\tilde{B}\,^2B_2$ relaxation. A dramatic loss of correlation occurs within one period of ν_2 motion, which we associate with the first rapid curve-crossing process. The subsequent decay of the correlation occurs on the time scale of the ν_2 periods of motion, which we relate to the second curve-crossing process. At longer times the residual correlation is associated with those states whose trajectories do not move in the vicinity of the intersecting seam, and whose transition probabilities are correspondingly lower. The single caveat in this interpretation is that those levels which lie closest to the region of conical intersection, possessing ionization potentials of 17.44–18.00 eV, are predicted to be the most perturbed, yet appear to be the least perturbed levels in the energy spectrum. This inconsistency may be resolved if the energy minimum of the conical intersection is increased by ~ 0.3 eV or if significant Fermi interaction also occurs in this spectral region.

The intramolecular dynamics of the $\tilde{B}\,^2B_2$ state ions are undoubtedly complex in this femtosecond regime, where the kinetic behavior of the molecule is not firmly established. The excited-state ions are likely to succumb to more than one relaxation process. The correlation functions indicate, however, that the decay of the wave packet occurs on a 10^{-14} s time scale and is governed by the ν_2 motion. This suggests that the $\tilde{B}\,^2B_2$–$\tilde{A}\,^2A_1$ curve crossing dominates the femtosecond relaxation dynamics of H_2O^+ and D_2O^+.

V. CONCLUSIONS

High resolution photoelectron spectroscopy has been performed on supersonic molecular beams of H_2O and D_2O. The rotational cooling and a least squares fitting procedure, employing empirical instrument response functions, have enabled spectroscopic constants of improved accuracy to be evaluated for the $\tilde{X}\,^2B_1$ and $\tilde{A}\,^2A_1$ state ions. Values for ω_1^0, ω_2^0, and the quadratic anharmonicity constants x_{11}^0, x_{12}^0, and x_{22}^0 are reported. The $\tilde{B}\,^2B_2$ state photoelectron bands were simulated with anharmonic combination progressions in the symmetry-allowed modes ν_1 and ν_2. The general shape of the H_2O^+ and D_2O^+ bands could be described by this simple simulation, but the measured level density could not be reproduced. This is particularly evident for the ions with >0.6 eV internal energies.

Autocorrelation functions were calculated from the photoelectron bands for all three electronic states. The ground $\tilde{X}\,^2B_1$ state correlation functions display oscillatory patterns, which are characteristic of virtually undisplaced wave packets composed of two oscillators. In the case of the $\tilde{A}\,^2A_1$ state correlation function, a rapid dephasing of the wave packet is observed. This effect is attributed to the Renner–Teller coupling between the $\tilde{A}\,^2A_1$ vibronic sublevels with $K>0$ and the $\tilde{X}\,^2B_1$ state. The $\tilde{B}\,^2B_2$ state correlation function for each ion exhibits an ultrafast decay. Following the initial wave packet dephasing and commensurate loss of correlation through intramolecular energy transfer, the correlation functions of both H_2O^+ and D_2O^+ continue to decay on a time scale equal to one period of ν_2 bending motion. This decay pattern supports the curve-crossing model for $\tilde{B}\,^2B_2$ state relaxation, which involves a conical intersection between the $\tilde{A}\,^2A_1$ and $\tilde{B}\,^2B_2$ potential energy surfaces. The nonadiabatic $\tilde{B}\,^2B_2 \rightarrow \tilde{A}\,^2A_1$ transition probability is expected to be promoted by the ν_2 motion and occur on a 10^{-14} s time scale.

ACKNOWLEDGMENTS

This work was supported by the Director, Office of Energy Research, Office of Basic Energy Sciences, Chemical Sciences Division of the U. S. Department of Energy under Contract No. DE-AC03-76SF00098.

[1] H. Lew, Can. J. Phys. **54**, 2028 (1976).
[2] W. Meyer, Int. J. Quantum Chem. Symp. **5**, 341 (1971).
[3] J. A. Smith, P. Jørgenson, and Y. Öhrn, J. Chem. Phys. **62**, 1285 (1975).
[4] P. C. Hariharan and J. A. Pople, Mol. Phys. **27**, 209 (1974).
[5] P. J. Fortune, B. J. Rosenberg, and A. C. Wahl, J. Chem. Phys. **65**, 2201 (1976).
[6] C. R. Brundle and D. W. Turner, Proc. R. Soc. London Ser. A **307**, 27 (1968).
[7] R. N. Dixon, G. Duxbury, J. W. Rabalais, and L. Asbrink, Mol. Phys. **31**, 423 (1976).
[8] L. Karlsson, L. Mattsson, R. Jadrny, R. G. Albridge, S. Pinchas, T. Bergmark, and K. Siegbahn, J. Chem. Phys. **62**, 4745 (1975).
[9] P. L. Kronebusch and J. Berkowitz, Int. J. Mass Spectrom. Ion Phys. **22**, 283 (1976).
[10] G. R. Mohlmann, K. K. Bhutani, F. J. DeHeer, and S. Tsurubuchi, Chem. Phys. **31**, 273 (1978).
[11] J. Brzozowski, P. Erman, and H. Lew, Chem. Phys. Lett. **34**, 267 (1975).
[12] F. Fiquet-Fayard and P. M. Guyon, Mol. Phys. **11**, 17 (1966).
[13] A. J. Lorquet and J. C. Lorquet, Chem. Phys. **4**, 353 (1974).
[14] J. H. D. Eland, Chem. Phys. **11**, 41 (1975).
[15] G. G. Balint-Kurti and R. N. Yardley, Chem. Phys. Lett. **36**, 342 (1975).
[16] C. F. Jackels, J. Chem. Phys. **72**, 4873 (1980).
[17] R. A. Rouse, J. Chem. Phys. **64**, 1224 (1976).
[18] D. Dehareng, X. Chapuisat, J.-C. Lorquet, C. Galloy, and G. Raseev, J. Chem. Phys. **78**, 1246 (1983).
[19] J. E. Pollard, D. J. Trevor, Y. T. Lee, and D. A. Shirley, Rev. Sci. Instrum. **52**, 1837 (1981).
[20] C. M. Truesdale, S. Southworth, P. H. Kobrin, D. W. Lindle, G. M. Thornton, and D. A. Shirley, J. Chem. Phys. **76**, 860 (1982).
[21] A. Lofthus and P. H. Krupenie, J. Phys. Chem. Ref. Data **6**, 113 (1976).
[22] *Atomic Energy Levels*, edited by Charlotte E. Moore, Natl. Stand. Ref. Data Ser. Natl. Bur. Stand. (U. S. GPO, Washington, D.C., 1958), Vols. I and II.
[23] E. J. Heller, Acc. Chem. Res. **14**, 368 (1981), and references therein.
[24] A. J. Lorquet, J. C. Lorquet, J. Delwiche, and M. J. Hubin-Franskin, J. Chem. Phys. **76**, 4692 (1982).
[25] J. E. Pollard, D. J. Trevor, J. E. Reutt, Y. T. Lee, and D. A. Shirley, J. Chem. Phys. **81**, 5302 (1984).
[26] J. E. Reutt, L. S. Wang, J. E. Pollard, D. J. Trevor, Y. T. Lee, and D. A. Shirley, J. Chem. Phys. **84**, 3022 (1986).

[27]J. Wayne Rabelais, *Principles of Ultraviolet Photoelectron Spectroscopy* (Wiley, New York, 1977).
[28]E. Oran Brighan, *The Fast Fourier Transform* (Prentice–Hall, Englewood Cliffs, 1974), p. 164.
[29]Gerhard Herzberg, *Molecular Spectra and Molecular Structure. III. Infrared and Raman Spectra of Polyatomic Molecules* (Van Nostrand Reinhold, New York, 1945).
[30]Ch. Jungen and A. J. Merer, *Molecular Spectroscopy, Modern Research*, edited by K. Narahan Rao (Academic, New York, 1976), Vol. II, p. 127.
[31]K. Dressler and D. A. Ramsay, Philos. Trans. R. Soc. London Ser. A **251**, 69 (1959).